

# Luminescent Properties of LaPO<sub>4</sub>:Eu Nanoparticles and Nanowires

Lixin Yu, Hongwei Song,\* Shaozhe Lu, Zhongxin Liu, Linmei Yang, and Xianggui Kong

Key Laboratory of Excited-State Physics, Changchun Institute of Optics, Fine Mechanics and Physics, Chinese Academy of Sciences, 16 Eastern South-Lake Road, Changchun 130033, P. R. China

Received: May 27, 2004; In Final Form: August 22, 2004

Nanoparticles (NPs) and nanowires (NWs) as well as micrometer particles (MPs) and micrometer rods (MRs) of LaPO<sub>4</sub>:Eu phosphors were synthesized by the hydrothermal method. Their luminescent properties, including local symmetry surrounding Eu<sup>3+</sup> ions and electronic transition processes, were studied and compared. The results indicated that, in NPs and MPs, Eu<sup>3+</sup> occupied only one site, A, while in NWs and MRs, Eu<sup>3+</sup> occupied the same site, A, and an additional site, B. Varying from NWs to MRs, the relative emission intensity of Eu<sup>3+</sup> ions at site B was reduced. The radiative transition rates of <sup>5</sup>D<sub>1</sub>– $\sum_j$ <sup>7</sup>F<sub>j</sub> and nonradiative transition rates of <sup>5</sup>D<sub>1</sub>–<sup>5</sup>D<sub>0</sub> in different powders were obtained by measuring temperature-dependent luminescent dynamics. The results indicated that the radiative transition rate of <sup>5</sup>D<sub>1</sub>– $\sum_j$ <sup>7</sup>F<sub>j</sub> in NWs increased 1.5–1.8 times over that in NPs, MPs, and MRs, while the nonradiative transition rates had only a little variation. Thereby, the luminescent quantum efficiency (QE) of <sup>5</sup>D<sub>1</sub> at 0 K in NPs, NWs, MPs, and MRs was deduced to be 38%, 59%, 49%, and 47%, respectively. The radiative transition rate of <sup>5</sup>D<sub>0</sub>– $\sum_j$ <sup>7</sup>F<sub>j</sub> in NWs also increased ~1.5 times. The increase of the radiative electronic transition rate in NWs was attributed to the variation of dipole field caused by the shape anisotropy.

## Introduction

It is well-known that reduction of the particle size in a crystalline system can result in remarkable modifications of properties, which are different from those of the bulk because of a high surface-to-volume ratio and the quantum confinement effect of nanometer materials. In 1994, Bhargava et al. reported that the radiative transition rate of ZnS:Mn nanocrystals increased 5-fold in comparison with that of the bulk.<sup>1</sup> Despite the fact that this result was strongly criticized later, the studies on nanosized luminescent semiconductors have attracted great interest.<sup>2–4</sup> Rare earth (RE) compounds were extensively applied in luminescence and display, such as lighting, field emission display (FED), cathode ray tubes (CRT), and plasma display panels (PDP).<sup>5–9</sup> It is expected that nanosized RE compounds can increase luminescent QE and display resolution. To improve luminescent properties of nanocrystalline phosphors, many preparation methods have been used, such as solid-state reactions, sol–gel techniques, hydroxide precipitation, hydrothermal synthesis, spray pyrolysis, laser-heated evaporation, and combustion synthesis.<sup>10–13</sup> Currently, the luminescent RE-doped one-dimensional nanocrystals such as LaPO<sub>4</sub>:RE NWs and Y<sub>2</sub>O<sub>3</sub>:RE nanotubes have also attracted considerable interest.<sup>14,15</sup> Moreover, in comparison with zero-dimensional NPs, the shape anisotropy of a one-dimensional structure provided a better model system to investigate the dependence of electronic transport and optical properties on size confinement and dimensionality. However, until now, their luminescent properties did not compare well to the zero-dimensional NPs. To develop one-dimensional phosphors, a basic question should be answered: Could the photoluminescent properties for one-dimensional nanocrystals be improved over those of zero-dimensional nanocrystals, as well as micrometer materials, the so-called bulk materials?

Lanthanide orthophosphate (LnPO<sub>4</sub>) belongs to two polymorphic types, the monoclinic monazite type (for La to Gd) and the quadratic xenotime type (for Tb to Lu). Because of its high QE, bulk lanthanide phosphate as an ideal host in fluorescent lamps, CRTs, and PDPs has been intensively investigated.<sup>16–18</sup> However, the reports on lanthanide phosphate as nanocrystals doped with RE ions are quite rare.<sup>14,19</sup> In 1999, Meyssamy et al. synthesized LaPO<sub>4</sub>:Eu and LaPO<sub>4</sub>:Tb nanocrystals (NPs and NWs) for the first time and reported their luminescent properties at room temperature.<sup>14</sup> We consider that their luminescent characteristics such as local symmetry, electronic transition processes, and surface effects should be discussed further. Especially, the spectral differences between NWs and NPs should be revealed. On the basis of this consideration, we prepared LaPO<sub>4</sub>:Eu NPs and NWs, as well as the corresponding MPs and MRs, by the same method. In this paper, the luminescent properties, including the electronic transition processes and the local symmetry surrounding Eu<sup>3+</sup> ions have been systemically studied and compared.

## Experiments

**Sample Preparation.** In the preparation of NPs, appropriate amounts of high-purity La<sub>2</sub>O<sub>3</sub> and Eu<sub>2</sub>O<sub>3</sub> (1:0.05 in mole ratio) were dissolved into concentrated HNO<sub>3</sub> first, and the appropriate volume of deionized water was added. Then, an appropriate volume of NaOH aqueous solution (0.05 M) and (NH<sub>4</sub>)<sub>2</sub>HPO<sub>4</sub> aqueous solution (0.18 M) were added to the solution. The final pH value was adjusted to 12–13 with NaOH solution (4 M). After thorough stirring, the milky colloidal solution was poured into several closed, Teflon-lined autoclaves and subsequently heated at 120 °C for 3 h. The obtained suspension was centrifuged at 2770 g for 15 min, and the supernatant was discarded. Then, the precipitate was dissolved in a dilute HNO<sub>3</sub> solution, and the pH value was adjusted to 1.0. The mixture was stirred for 3 h in order to dissolve La(OH)<sub>3</sub>. The white

\* Corresponding author. Fax: 86-431-6176320. E-mail: songhongwei2000@sina.com.cn.

**TABLE 1: List of the Concentration of  $\text{Eu}^{3+}$  Ions in Different Samples**

sample	doped concentration	practical concentration
NPs	5%	4.15%
NWs	5%	4.32%
MPs	5%	4.36%
MRs	5%	4.41%

suspension obtained was centrifuged at 2770 g for 15 min. The colorless supernatant containing byproducts was discarded. To separate nanoparticles from micrometer particles, an appropriate quantity of deionized water was added into the white precipitate with stirring and then centrifuged at 2770 g for 10 min; the supernatant containing nanoparticles was decanted. This process was repeated four times. The resultant colloidal solution was dried at 50 °C at vacuum condition.

In the preparation of NWs, appropriate amounts of  $\text{La}_2\text{O}_3$  and  $\text{Eu}_2\text{O}_3$  were dissolved in concentrated  $\text{HNO}_3$ , and an appropriate volume of deionized water was added into it. An aqueous solution of  $(\text{NH}_4)_2\text{HPO}_4$  (0.20 M) was added. The pH value of the resultant solution was adjusted to 1.0 with dilute  $\text{HNO}_3$  (1.0 M) solution. Other preparations followed the same procedures.

In comparison, bulk  $\text{LaPO}_4\text{:Eu}$  powders were also prepared by the same method at 150 °C. A practical concentration of  $\text{Eu}^{3+}$  ions in the matrix was obtained by inductivity-coupled plasma atomic emission spectroscopy, as shown in Table 1. The results indicated that the practical content of  $\text{Eu}^{3+}$  in different samples was almost same and had little decrease in comparison to the starting content.

**Measurements.** Crystal structure, morphology, and size were obtained by X-ray diffraction (XRD) using a Cu target radiation resource ( $\text{Cu K}\alpha = 1.54078 \text{ \AA}$ ), transmission electron microscopy (TEM) utilizing a JEM-2010 electron microscope, and scanning electron microscopy (SEM) using a JSM-5500 electron microscope.

The excitation and emission spectra at room temperature were measured with a Hitachi F-4500 fluorescence spectrometer. In the measurements of low-temperature, high-resolution spectra and temperature-dependent fluorescent dynamics, the samples were put into a liquid-helium-cycling system, where the temperature varied from 10 to 300 K. A 266-nm light generated from the fourth harmonic generator pumped by the pulsed Nd:YAG laser was used as general excitation source. A Rhodamine 6G dye pumped by the same Nd:YAG laser was used as a site-selective excitation source. The Nd:YAG laser operated with a line width of  $1.0 \text{ cm}^{-1}$ , pulse duration of 10 ns, and repetition frequency of 10 Hz. The spectra and dynamics were recorded by a Spex 1403 spectrometer, a photomultiplier, and a boxcar integrator and processed by a computer.

## Results and Discussion

**A. Crystal Structure and Morphology.** Figure 1 shows TEM images of nanosized  $\text{LaPO}_4\text{:Eu}$  NPs and NWs and SEM images of MPs and MRs. As can be seen from TEM and SEM, the morphology of the samples was different on the basis of the solution pH value at the synthesis process: NPs/MPs were basic, and NWs/MRs were acidic. The size of the  $\text{LaPO}_4\text{:Eu}$  NPs ranges from 10 to 20 nm. The diameter of the  $\text{LaPO}_4\text{:Eu}$  NWs ranges from 10 to 20 nm, and the length ranges several hundred nanometers. The high-resolution transmission electron micrograph (HRTEM) images showed that the inside of NWs were well-crystallized, and the fringe had degenerated. The electron diffraction patterns also showed that the NWs were

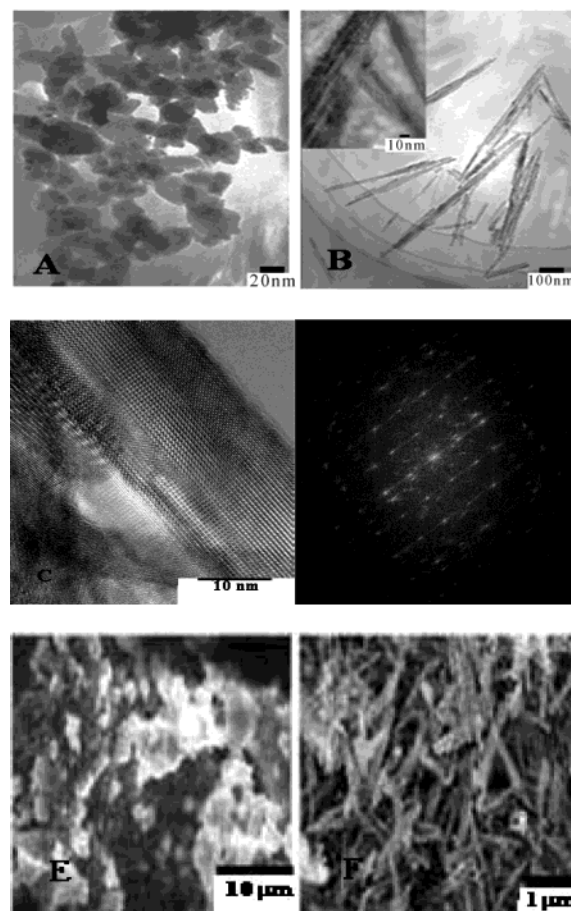


**Figure 1.** TEM and SEM images of  $\text{LaPO}_4\text{:Eu}$  samples. (part A) TEM of NPs, (part B) TEM of NWs, (part C) HRTEM of NWs, (part D) electron diffraction of NWs, (part E) SEM of MPs, (part F) SEM of MRs.

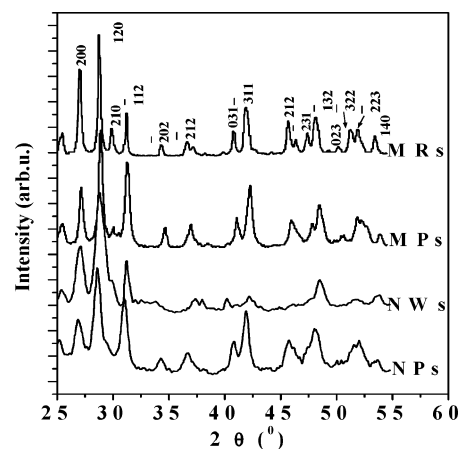


**Figure 2.** XRD patterns of  $\text{LaPO}_4\text{:Eu}$  NPs, NWs, and bulk samples.

single crystals. The size depended on the preparation temperature. As the preparation temperature was elevated to 150 °C, the particles were formed in basic solution, with a diameter of 1–2  $\mu\text{m}$ , while the MRs were formed in acidic condition, with a width of  $\sim 200 \text{ nm}$  and a length of 1–2  $\mu\text{m}$ .

Figure 2 shows the XRD patterns of  $\text{LaPO}_4\text{:Eu}$  NPs, NWs, MPs, and MRs. Like the bulk  $\text{LaPO}_4$  polycrystals prepared with the solid reaction, the crystal structures of the samples all belong to the monoclinic monazite type.<sup>20,21</sup> No additional phase was formed. In comparison to the other samples, the relative intensity of some diffraction peaks for the NWs (40–55) obviously

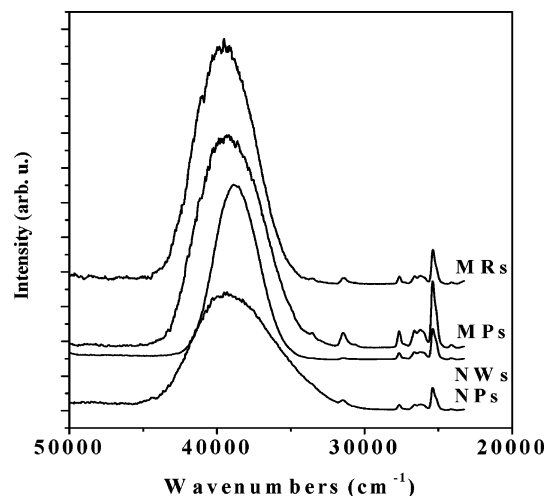


**Figure 3.** Excitation spectra of bulk LaPO<sub>4</sub>:Eu powders, NPs, and NWs ( $\lambda_{\text{em}} = 16\,393\text{ cm}^{-1}$ ).

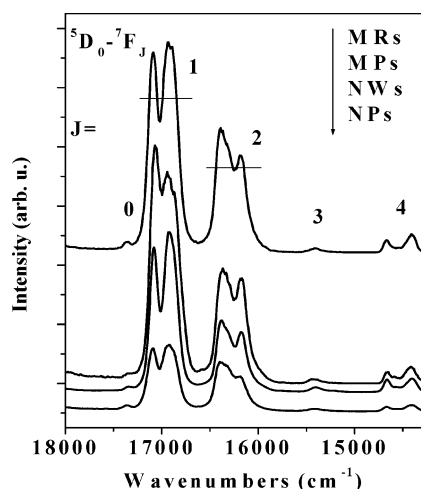


**Figure 4.** Emission spectra of bulk LaPO<sub>4</sub>:Eu powders ( $\lambda_{\text{ex}} = 39\,525\text{ cm}^{-1}$ ), NPs ( $\lambda_{\text{ex}} = 39\,525\text{ cm}^{-1}$ ), and NWs ( $\lambda_{\text{ex}} = 38\,610\text{ cm}^{-1}$ ).

decreased. This was attributed to the improved shape anisotropy. A similar phenomenon was observed in potassium titanate NWs.<sup>22</sup>

**B. Excitation and Emission Spectra.** Figure 3 shows the excitation spectra at  $19\,393\text{ cm}^{-1}$  in different LaPO<sub>4</sub>:Eu samples. In Figure 3, the wide band extending from  $45\,000$  to  $34\,000\text{ cm}^{-1}$  was associated with the charge transfer (CT) transition from the  $2p$  orbital of  $\text{O}^{2-}$  ions to the  $4f$  orbital of  $\text{Eu}^{3+}$  ions, while the sharp lines are associated with the direct excitation of the  $f-f$  shell transitions of  $\text{Eu}^{3+}$ . T. Igrashi et al. reported that in  $\text{Y}_2\text{O}_3:\text{Eu}$  NPs, the CT band blue-shifted as the particle size decreased, and we observed that the intensity of the CT band in NPs decreased by UV light irradiation.<sup>23,24</sup> In Figure 3, the peak locations of the CT band in NPs, NWs, MPs, and MRs were  $39\,556$ ,  $38\,610$ ,  $39\,525$ , and  $39\,525\text{ cm}^{-1}$ , respectively. The peak location of the CT band in the NPs had no shift in comparison with that in the bulk powders, while that in the NWs red-shifted. It should be pointed out that, as in  $\text{Y}_2\text{O}_3:\text{Eu}^{3+}$  NPs, the intensity of the CT band in LaPO<sub>4</sub>:Eu<sup>3+</sup> NPs and NWs also decreased by UV light irradiation, which was attributed to local structural change surrounding  $\text{Eu}^{3+}$  ions at/near the surface.<sup>24</sup>

Figure 4 shows the emission spectra of different LaPO<sub>4</sub>:Eu powders at room temperature. The  $^5\text{D}_0-^7\text{F}_J$  transitions ( $J = 0, 1, 2, 3, 4$ ) were observed, as labeled in the figure. Among them, the  $^5\text{D}_0-^7\text{F}_1$  transitions were the strongest. The intensity ratio

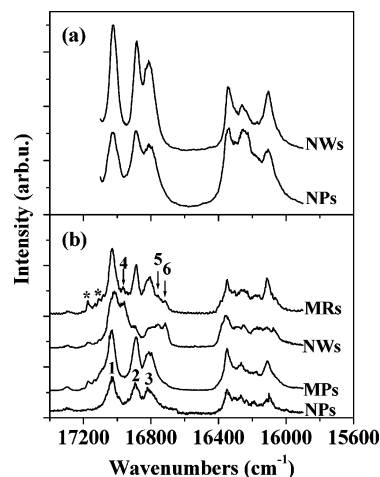


**Figure 5.** High-resolution spectra of LaPO<sub>4</sub>:Eu bulk, NPs, and NWs at room temperature (part a) and at 10 K (part b) under 266-nm light excitation (delay time is  $50\text{ }\mu\text{s}$ ).

of  $^5\text{D}_0-^7\text{F}_2$  to  $^5\text{D}_0-^7\text{F}_1$  varied depending on the morphology of the powders. In Figure 4, the intensity ratios of  $^5\text{D}_0-^7\text{F}_2$  to  $^5\text{D}_0-^7\text{F}_1$  in NPs, NWs, MPs, and MRs were determined to be 0.81, 0.57, 0.88, and 0.58, respectively. As is well-known, the  $^5\text{D}_0-^7\text{F}_1$  lines originate from magnetic dipole transition, while the  $^5\text{D}_0-^7\text{F}_2$  lines originate from electric dipole transition. In terms of the Judd–Ofelt theory,<sup>25,26</sup> the magnetic dipole transition is permitted. The electric dipole transition is allowed only on the condition that the europium ion occupies a site without an inversion center and is sensitive to local symmetry. Subsequently, when  $\text{Eu}^{3+}$  ions occupy inversion center sites, the  $^5\text{D}_0-^7\text{F}_1$  transition should be relatively strong, while the  $^5\text{D}_0-^7\text{F}_2$  transition should be relatively weak. The results stated already indicate that, in the NWs and MRs, more  $\text{Eu}^{3+}$  ions occupy inversion center sites in comparison with the spherical particles.

**C. High-Resolution Spectra and Site Symmetry.** As mentioned already, LaPO<sub>4</sub> belongs to the monazite type. In LaPO<sub>4</sub> systems,  $\text{La}^{3+}$  ions occupy  $C_1$  point group. In  $\text{Eu}^{3+}$ -doped LaPO<sub>4</sub>,  $\text{Eu}^{3+}$  ions substitute for some of  $\text{La}^{3+}$  ions. The spectroscopy of  $\text{Eu}^{3+}$  ions in bulk LaPO<sub>4</sub> was studied by J. Dexter-Ghys et al. in detail.<sup>17</sup> Figure 5 shows the high-resolution spectra of LaPO<sub>4</sub>:Eu NPs, NWs, MPs, and MRs under 266-nm excitation at room temperature (Figure 5a) and 10 K (Figure 5b). It can be seen that the room temperature spectra are nearly the same for NPs and NWs. The transition energies of the peaks have been calculated and are in good agreement with the spectral positions observed in the bulk materials.<sup>17</sup> This indicates that the  $\text{Eu}^{3+}$  ions in NWs and NPs have the same symmetry,  $C_1$ . The emission associated with  $^5\text{D}_0-^7\text{F}_1$  transitions is quite different between NPs and NWs at 10 K. In the NPs, three  $^5\text{D}_0-^7\text{F}_1$  emission lines were observed, locating at  $17\,025 \pm 2\text{ cm}^{-1}$  (L1),  $16\,898 \pm 2\text{ cm}^{-1}$  (L2), and  $16\,815 \pm 2\text{ cm}^{-1}$  (L3). In the NWs, besides the same lines L1–3, three additional lines L4–6 were observed, locating at  $16\,963 \pm 2\text{ cm}^{-1}$  (L4),  $16\,758 \pm 2\text{ cm}^{-1}$  (L5), and  $16\,718 \pm 2\text{ cm}^{-1}$  (L6). The  $^5\text{D}_0-^7\text{F}_1$  lines in the MPs were entirely identical with those in the NPs, indicating that site symmetry in MPs was the same as that in NPs. For the MRs, lines L1–6 were also observed. However, the relative intensities of lines L4–6 became weaker in comparison to those in NWs. As is known, the  $^5\text{D}_0-^7\text{F}_1$  emissions are hypersensitive to the crystal field.  $^7\text{F}_1$  associated with one site symmetry can split into three Stark lines in the crystal field. The results in Figure 5 indicated that, in NPs and MPs, the  $^5\text{D}_0-^7\text{F}_1$  transitions



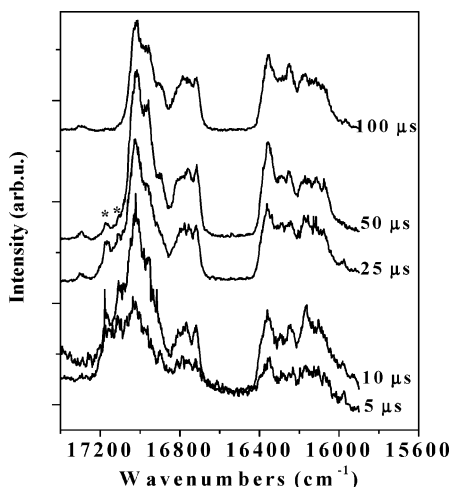


**Figure 6.** The time-resolved emission spectra of NWs for different delay times at 10 K.

came from one crystalline site, A, while in NWs and MRs, the  $^5D_0$ – $^7F_1$  transitions came from the same site (L1–3), A, and an additional site (L4–6), B. The relative number of  $\text{Eu}^{3+}$  at site B decreased as the powders varied from the NWs to the MRs.

Some authors reported the appearance of additional sites of  $\text{Eu}^{3+}$  in nanocrystals due to the surface effect.<sup>9,15,27</sup> In the present case, from the MPs to the NPs (20 nm), the ratio of surface to volume increased greatly, but no additional site was observed. From the MRs to the NWs, the ratio of surface to volume did not increase so much; however, the additional site B appeared, and the relative number of  $\text{Eu}^{3+}$  at site B changed greatly. We thus believe that the appearance of the additional site B is not caused by the surface effect but by the shape anisotropy. In wirelike nanocrystals, as can be seen from TEM images, the atomic alignments between the fringe range and internal range are different, leading to the degeneration of the crystal field in the fringe range and the appearance of the new site B. The ratio of length to diameter in the MRs is 5–10, while that in the NWs increases to 30. The increased shape anisotropy leads to the increase of the number of site B.

It should be pointed out that, in Figure 5, the peaks labeled with a star (\*) are not associated with the  $^5D_0$ – $^7F_1$  transitions but with some  $^5D_1$ – $^7F_j$  transitions. This was identified by time-resolved emission spectra. Figure 6 shows the time-resolved emission spectra (5–100  $\mu\text{s}$ ) in NWs corresponding to  $^5D_0$ – $^7F_j$  transitions. It can be seen that as the delay time increased from 5 to 100  $\mu\text{s}$ , the intensity of the peaks labeled with a star (\*) decreased dramatically and nearly disappeared, indicating that the lifetime for these peaks was on the order of several 10  $\mu\text{s}$ . This was very consistent with the decay time constant of  $^5D_1$ . The emission intensities of the other peaks originating from  $^5D_0$  had only a little variation, because the lifetime of  $^5D_0$  is on the order of several milliseconds. According to the energy separation between  $^7F_j$ 's, we concluded that the labeled peaks originated from  $^5D_1$ – $^7F_3$ .

The  $^5D_0$ – $^7F_2$  transitions of  $\text{Eu}^{3+}$  at one site can split into, at most, five lines in the crystal field. In Figure 5, the emission spectra at room temperature between NPs and NWs demonstrate no obvious differences. The low-temperature spectra between NPs and NWs demonstrate obscure differences, because the peaks broadened and were not completely split. To identify further, the site-selective spectroscopy was studied. Figure 7a and b shows, respectively, the  $^7F_0$ – $^5D_0$  excitation spectra monitoring different  $^5D_0$ – $^7F_2$  sites and the  $^5D_0$ – $^7F_2$  emission

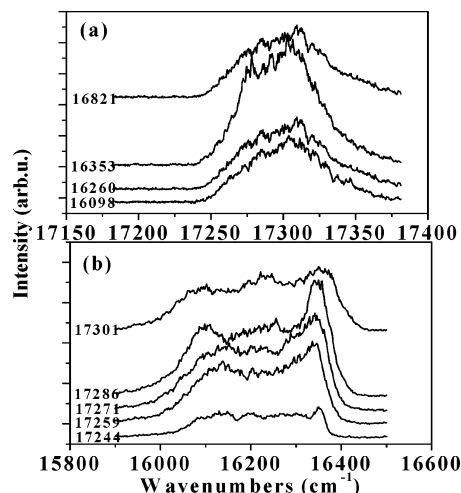


**Figure 7.** (part a)  $^7F_0$ – $^5D_0$  excitation spectra monitoring different sites and (part b) site-selective emission spectra of  $\text{LaPO}_4:\text{Eu}$  NPs at 10 K (delay time is 50  $\mu\text{s}$ ).

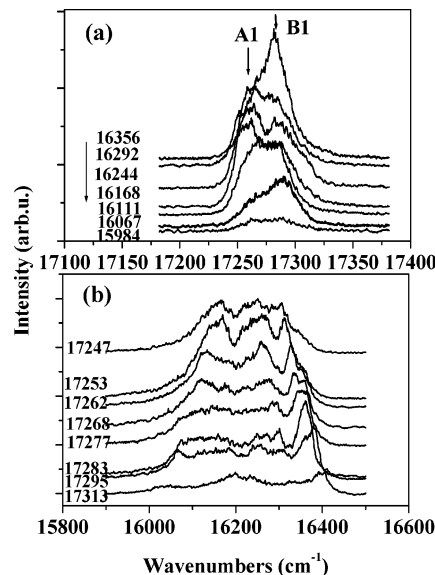


**Figure 8.** (part a)  $^7F_0$ – $^5D_0$  excitation spectra monitoring different sites and (part b) site-selective emission spectra of  $\text{LaPO}_4:\text{Eu}$  NWs at 10 K (delay time is 50  $\mu\text{s}$ ).

spectra selectively exciting  $^7F_0$ – $^5D_0$  transitions in the NPs. In Figure 7a, only one excitation line was observed. The peak location of the line had only a little shift, and the spectral configuration almost did not change as it monitored different  $^5D_0$ – $^7F_2$  emission sites. In Figure 7b, from the spectral configuration, four lines were distinguished. These results indicate that, in NPs, the  $^5D_0$ – $^7F_2$  transitions also originated from one symmetry site. Figure 8a and b shows, respectively, the  $^7F_0$ – $^5D_0$  excitation spectra monitoring different  $^5D_0$ – $^7F_2$  sites and the  $^5D_0$ – $^7F_2$  emission spectra selectively exciting  $^7F_0$ – $^5D_0$  transitions in NWs. In Figure 8a, two different excitation peaks were observed, at  $\sim 17\,261$  (A1) and  $17\,281$  (B1)  $\text{cm}^{-1}$ , which correspond to two different symmetry sites. As selectively exciting A1 and B1, two group emission lines of  $^5D_0$ – $^7F_2$  appeared. It can be seen that, corresponding to site A1, the separation between the Stark splitting lines is smaller, while corresponding to site B1, the energy separation is larger. This implies that  $\text{Eu}^{3+}$  ions at site B1 were interacting with a stronger crystal field.

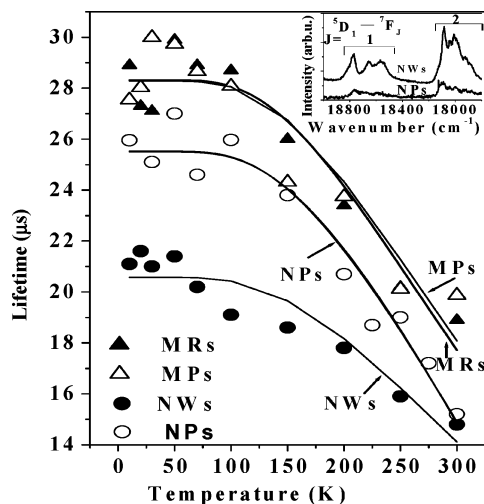


**Figure 9.** Dependence of fluorescence lifetime of  $^5D_1-^7F_2$  on temperature. Scattered dots are experimental data, and solid lines are fitting lines. Inset: emissions of  $^5D_1-^7F_j$  transitions (delay time is 50  $\mu$ s).

**D. Electronic Transition Rates of Eu<sup>3+</sup> in Different Powders.** The  $^5D_1$  level is an intermediate excited state among  $^5D_j$ 's and is suitable to analyze radiative and nonradiative transition processes. Under the 266-nm excitation, electrons from the ground state were excited to the CT state first and then were fed to excited  $^5D_j$  states. The electrons in the  $^5D_1$  state came from the nonradiative CT state feeding and  $^5D_2-^5D_1$  relaxation. The CT state S feeding of  $^5D$  is faster than the decay of  $^5D$ . We assume that the depopulation processes in  $^5D_1$  were contributed mainly to the radiative  $^5D_1-\sum_j^7F_j$  transitions and the one-step nonradiative  $^5D_1-^5D_0$  transition. The nonradiative relaxation is a multiphonon process. Then, the lifetime of  $^5D_1$  can be expressed as<sup>28</sup>

$$\tau(T) = \frac{1}{W_1 + W_{10}(T)} \quad (1)$$

where  $W_1$  is the radiative transition rate of  $^5D_1-\sum_j^7F_j$ , and  $W_{10}(T)$  is the nonradiative transition rate at a certain temperature,  $T$ . Here, the cross-relaxation process between Eu<sup>3+</sup> ions was omitted, because the lifetime hardly changed for different Eu<sup>3+</sup> concentrations. According to the theory of multiphonon relaxation,  $W_{10}$  can be written as

$$W_{10}(T) = W_{10}(0)(1 + \langle n \rangle)^{\Delta E_{10}/\hbar\omega} \quad (2)$$

where  $W_{10}(0)$  is nonradiative transition rate at 0 K,  $\Delta E_{10}$  is the energy separation between  $^5D_1$  and  $^5D_0$ ,  $\hbar\omega$  is the phonon energy,  $k$  is Boltzmann's constant, and  $\langle n \rangle = 1/(e^{\hbar\omega/kT} - 1)$  is the phonon occupation number. According to eqs 1–2, the lifetime of  $^5D_1$  can be expressed as

$$\tau = \frac{1}{W_1 + W_{10}(0)[1 - \exp(-\hbar\omega/kT)]^{-\Delta E_{10}/\hbar\omega}} \quad (3)$$

According to eq 3, if the fluorescence lifetime as a function of temperature is measured, then  $W_1$  and  $W_{10}$  can be obtained by fitting.

The fluorescence decay curves of  $^5D_1-^7F_2$  as well as  $^5D_0-^7F_2$  monitoring the same site were measured at different temperatures. The  $^5D_1-^7F_2$  and  $^5D_0-^7F_2$  emissions both decayed exponentially, measuring at different temperatures. Figure 9 shows the dependence of  $^5D_1-^7F_2$  exponential lifetimes on

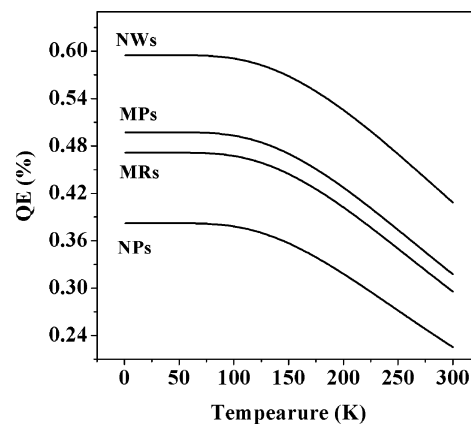


**Figure 10.** Dependence of QE for the  $^5D_1$  level on temperature.

**TABLE 2: List of Parameters  $W_1$ ,  $W_{10}(0)$ , and the Internal Luminescent QE at 0 K in Different Powders**

parameter	NPs	NWs	MPs	MRs
$W_1$ (ms <sup>-1</sup> )	14.9	28.9	17.6	16.5
$W_{10}$ (ms <sup>-1</sup> )	24.1	19.7	17.8	18.5
QE	38%	59%	49%	47%

temperature. The inset gives the fluorescence spectra of  $^5D_1-^7F_j$  ( $J = 1, 2$ ) transitions. It can be seen that the lifetimes of  $^5D_1-^7F_2$  in the MPs and MRs are nearly same. The lifetime in the NPs is shorter, and the lifetime in the NWs is the shortest. Below  $\sim 100$  K, the lifetime nearly became a constant. Above 100 K, the lifetime decreased rapidly with elevated temperature for all the samples. The experimental data were well fitted by eq 3. In the fitting, we chose  $\Delta E_{10} = 1758$  cm<sup>-1</sup> and  $\hbar\omega = 390$  cm<sup>-1</sup>. Actually, we measured the Raman scattering spectra of powders and observed that the 390 cm<sup>-1</sup> vibration mode was dominant in LaPO<sub>4</sub>. In addition, we also fitted the experimental dots in Figure 8, taking  $\hbar\omega$  as a variable parameter. The result indicated that  $\hbar\omega = 370$  cm<sup>-1</sup> was the best fitting parameter, which was close to 390 cm<sup>-1</sup>.

$W_1$  and  $W_{10}(0)$  in different powders were obtained, as listed in Table 2. The radiative transition rates in the MPs and MRs were almost the same. In comparison to the MPs and MRs, the radiative transition rate in the NPs decreased a little, while that in the NWs increased obviously. In comparison to the MPs and MRs, the nonradiative transition rate of  $^5D_1-^5D_0$  in NPs and NWs had a small increase. The internal luminescent QE for the  $^5D_1$  level at 0 K, determined by  $\eta = W_1/[W_1 + W_{10}(0)]$  was also listed in Table 2. According to fitting results by eq 3 and the QE formula, we calculated the QE as a function of temperature, drawn in Figure 10. It can be seen that the luminescent QE of  $^5D_1$  in NWs increased more than that in NPs, MPs, and MRs. The QEs in all samples decreased with the increase of temperature.

To determine the radiative and nonradiative transition rates of the  $^5D_0$  level, the fluorescence lifetimes of the  $^5D_0-^7F_2$  transitions as a function of temperature (10–300 K) in different samples were also measured. As the temperature varied from 10 to 300 K, the  $^5D_0$  lifetimes in all samples hardly changed. The  $^5D_0$  is the lowest excited state, and the energy separation between  $^5D_0$  and the nearest downlevel  $^7F_6$  is as high as  $\sim 12\,000$  cm<sup>-1</sup>. In this case, nonradiative relaxation processes hardly happen according to the theory of multiphoton relaxation. Similar results were also reported by Meltzer et al. in monoclinic Y<sub>2</sub>O<sub>3</sub>:Eu nanocrystals.<sup>7</sup> In cubic Y<sub>2</sub>O<sub>3</sub>:Eu nanocrystals prepared by combustion, it was observed that the fluorescence lifetime

**TABLE 3: List of  $^5\text{D}_0$  Lifetimes of  $\text{Eu}^{3+}$  in Different Samples at 10 and 300 K (monitoring position:  $16\,342\text{ cm}^{-1}$ )**

parameter	sample			
	NPs	NWs	MPs	MRs
lifetime at 10 K (ms)	2.30	1.70	2.34	2.41
lifetime at 300 K (ms)	2.25	1.63	2.32	2.40
radiative transition rate ( $\text{ms}^{-1}$ )	0.44	0.61	0.45	0.43

of  $^5\text{D}_0\text{--}^7\text{F}_2$  decreased as the temperature varied from 10 to 300 K.<sup>29</sup>

The lifetimes of  $^5\text{D}_0$  at 10 K and room temperature are listed in Table 3. Because the lifetimes of  $^5\text{D}_0$  almost do not vary with temperature, we have reason to suppose that the nonradiative transition rate can be neglected in comparison to the total radiative transition rate of  $^5\text{D}_0\text{--}\sum_j^7\text{F}_j$ . The lifetime at 10 K, as well as room temperature, is dominated by the radiative transition rate of  $^5\text{D}_0\text{--}\sum_j^7\text{F}_j$ . From Table 3, it can be seen that the radiative lifetime of  $^5\text{D}_0$  in NWs became shorter than that in NPs and bulk powders, and the radiative transition rate increased.

**E. Why the Electronic Transition Rate in NWs Can Be Improved.** For rare earth ions, the diameter of the wavefunction of the f electron is on the order of  $10^{-1}\text{ nm}$ , which is much smaller than the particle diameter, indicating the absence of the confinement effect. The increased radiative transition rate in NWs should not be caused by the crystal field. If the crystal field in the internal space of NWs was affected greatly in comparison to the other materials, the spectral shift of the  $^5\text{D}_0\text{--}^7\text{F}_1$  transitions for the same site A should be observed. However, the spectral positions for the site A in NWs did not vary in comparison to the other samples. In addition, the increased radiative transition rate should also be observed in the MRs, which have the same crystal structure and  $\text{Eu}^{3+}$  occupying two symmetry sites.

The increased radiative transition rate in NWs is related to shape anisotropy. The shape anisotropy will not influence the crystal field, but will influence the electric/magnetic dipole field caused by the excited ions. The dipole field is not only influenced by the typical dimensions and dielectric constants of the hosts but also their shape. We suggest that the anisotropy affects the ionic dipole field and, therefore, the photonic density states and the radiative transition rate. In the  $\text{LaPO}_4$  host, the transitions for  $\text{Eu}^{3+}$  include both the electronic dipole and magnetic dipole transitions.

In NPs and NWs, the nonradiative transition rate increased over that in the bulk powders and, in NPs, increased even more. This point is easily understood according to the surface effect. In NPs and NWs, the surface-to-volume ratio increased greatly over that in the bulk powder, and the surface-to-volume ratio in NPs increased even more. On the surface, a large number of surface defects exist, which act as nonradiative transition channels, leading the nonradiative transition rates to increase.

## Conclusions

NPs, NWs, MPs, and MRs of  $\text{LaPO}_4\text{:Eu}$  phosphors were successfully synthesized by the hydrothermal method and characterized by TEM/SEM graphs and XRD patterns. Their luminescent properties, especially the site symmetry and electronic transition processes, were systemically studied and compared by measuring the low-temperature, high-resolution spectra, site-selective excitation spectra, and temperature-dependent luminescent dynamics. The results indicate that, in NPs and MPs, despite the marked variability of particle size,  $\text{Eu}^{3+}$  occupied the same site, A, indicating that the size had no influence on local symmetry surrounding the  $\text{Eu}^{3+}$  ions. In NWs

and MRs,  $\text{Eu}^{3+}$  occupied not only site A but also an additional site, B. And in addition, from NWs to MRs, as the shape anisotropy decreased the relative emission intensity of  $\text{Eu}^{3+}$  at the site B decreased.

The electronic transition rates of  $^5\text{D}_1\text{--}\sum_j^7\text{F}_j$  and nonradiative transition rate of  $^5\text{D}_1\text{--}^5\text{D}_0$  were obtained. The results indicate that, in comparison to MPs and MRs, the radiative transition rates of  $^5\text{D}_1\text{--}\sum_j^7\text{F}_j$  in NPs were nearly the same, while those in NWs increased  $\sim 1.5$  times because of the shape anisotropy. A similar conclusion was also drawn for the emissions of  $^5\text{D}_0\text{--}\sum_j^7\text{F}_j$ . On the other hand, in comparison to MPs and MRs, the nonradiative transition rate of  $^5\text{D}_1\text{--}^5\text{D}_0$  in NPs increased largely because of improved surface-to-volume ratio, while that in NWs had little variation. The luminescent QE for the emission of  $^5\text{D}_1$  was deduced to be 38% in NPs, 59% in NWs, 49% in MPs, and 47% in MRs. This means that the QE for the  $^5\text{D}_1$  level of  $\text{Eu}^{3+}$  in NWs has improved over that in the bulk materials.

**Acknowledgment.** The authors gratefully thank the financial supports of the “One Hundred Talents Project” from the Chinese Academy of Sciences and Nation Natural Science Foundation of China (Grants 10374086 and 10274083).

## References and Notes

- Bhargava, R. N.; Gallagher, D.; Hong, X.; Nurmikko, A. *Phys. Rev. Lett.* **1994**, *72*, 416.
- Qadra, S. B.; Skelton, E. F.; Hsu, D.; Dinsmore, A. D.; Yang, J.; Gray, H. F.; Ratna, B. R. *Phys. Rev. B* **1999**, *60*, 9194.
- Ihara, M.; Igarashi, T.; Kusunoki, T.; Ohno, K. *J. Electrochem. Soc.* **2002**, *149*, H72.
- Donega, C. M.; Bol, A. A.; Meijerink, A. *J. Lumin.* **2002**, *96*, 87.
- Dhanaraj, J.; Jagannathan, R.; Kutty, T. N.; Lu, C. *J. Phys. Chem. B* **2001**, *105*, 11 098.
- Wei, Z.; Sun, L.; Liao, C.; Yan, C. *Appl. Phys. Lett.* **2002**, *80*, 1447.
- Meltzer, R. S.; Feofilov, S.; Tissue, B. M. *Phys. Rev. B* **1999**, *60*, R14 012.
- Williams, D. K.; Bihari, B.; Tissue, B. M.; McHale, J. M. *J. Phys. Chem. B* **1998**, *102*, 916.
- Hong, K. S.; Meltzer, R. S.; Bihari, B.; Williams, D. K.; Tissue, B. M. *J. Lumin.* **1998**, *76* and *77*, 234.
- Riwotzki, K.; Haase, M. *J. Phys. Chem. B* **1998**, *102*, 10 129.
- Bihari, B.; Eilers, H.; Tissue, B. M. *J. Lumin.* **1997**, *75*, 1.
- Bellessa, J.; Rabaste, S.; Plenet, J. C.; Mugnier, J.; Marty, O. *Appl. Phys. Lett.* **2001**, *79*, 2142.
- Hebbink, G. A.; Stouwdam, J. W.; Reinhoudt, D. N.; Veggel, C. *Adv. Mater.* **2002**, *14*, 1147.
- Meyssamy, H.; Riwoztki, K. *Adv. Mater. (Weinheim, Ger.)* **1999**, *11*, 840.
- Wu, C.; Qin, W.; Qin, G.; Zhao, D.; Zhang, J.; Huang, S.; Lu, S.; Liu, H.; Lin, H. *Appl. Phys. Lett.* **2003**, *82*, 520.
- Rambabu, U.; Amalnerkar, D. P.; Kale, B. B.; Buddhudu, S. *Mater. Chem. Phys.* **2001**, *70*, 1.
- Dexpert-Ghys, J.; Mauricot, R.; Faucher, M. D. *J. Lumin.* **1996**, *69*, 203.
- Wu, X.; You, H.; Gui, H.; Zeng, X.; Hong, G.; Kim, C.; Pyun, C.; Yu, B.; Park, C. *Mater. Res. Bull.* **2002**, *37*, 2531.
- Riwotzki, K.; Meyssamy, H.; Kornowski, A.; Haase, M. *J. Phys. Chem. B* **2000**, *104*, 2824.
- Rambabu, U.; Buddhudu, S. *Opt. Mater. (Amsterdam)* **2001**, *17*, 401.
- Munirathnam, U. R.; Prakash, T. L.; Buddhudu, S. *Mater. Phys. Chem.* **2003**, *78*, 160.
- Du, G. H.; Chen, Q.; Han, P. D.; Yu, Y.; Peng, L. M. *Phys. Rev. B* **2003**, *67*, 35 323.
- Igarashi, T.; Ihara, M.; Kusunoki, T.; Ohno, K. *Appl. Phys. Lett.* **2000**, *76*, 1549.
- Song, H.; Chen, B.; Peng, H.; Zhang, J. *Appl. Phys. Lett.* **2002**, *81*, 1776.
- Judd, B. R. *Phys. Rev.* **1962**, *127*, 750.
- Ofelt, G. S. *J. Chem. Phys.* **1962**, *37*, 511.
- Wei, Z.; Sun, L.; Liao, C.; Yin, J.; Jiang, X.; Yan, C. *J. Phys. Chem. B* **2002**, *106*, 10 610.
- Song, H.; Wang, J.; Chen, B.; Lu, S. *Chem. Phys. Lett.* **2003**, *376*, 1.
- Peng, H.; Song, H.; Chen, B.; Wang, J.; Lu, S.; Kong, X.; Zhang, J. *J. Chem. Phys.* **2003**, *118*, 3277.